

Ultrathin 2D/2D WO<sub>3</sub>/g-C<sub>3</sub>N<sub>4</sub> step-scheme H<sub>2</sub>-production photocatalystJunwei Fu<sup>a</sup>, Quanlong Xu<sup>a</sup>, Jingxiang Low<sup>a</sup>, Chuanjia Jiang<sup>b</sup>, Jiaguo Yu<sup>a,c,\*</sup><sup>a</sup> State Key Laboratory of Advanced Technology for Material Synthesis and Processing, Wuhan University of Technology, Wuhan, 430070, Hubei, PR China<sup>b</sup> College of Environmental Science and Engineering, Ministry of Education Key Laboratory of Pollution Processes and Environmental Criteria, Tianjin Key Laboratory of Environmental Remediation and Pollution Control, Nankai University, Tianjin, 300350, PR China<sup>c</sup> Faculty of Science, King Abdulaziz University, Jeddah, 21589, Saudi Arabia

## ARTICLE INFO

## Keywords:

Step-like photocatalyst  
 Step-scheme mechanism  
 S-Scheme heterojunction  
 Step heterojunction  
 Photocatalytic hydrogen generation

## ABSTRACT

The appropriate interfacial contact of heterojunction photocatalysts plays a critical role in transfer/separation of interfacial charge carriers. Design of two-dimensional (2D)/2D surface-to-surface heterojunction is an effective method for improving photocatalytic activity since greater contact area can enhance interfacial charge transfer rate. Herein, ultrathin 2D/2D WO<sub>3</sub>/g-C<sub>3</sub>N<sub>4</sub> step-like composite heterojunction photocatalysts were fabricated by electrostatic self-assembly of ultrathin tungsten trioxide (WO<sub>3</sub>) and graphitic carbon nitride (g-C<sub>3</sub>N<sub>4</sub>) nanosheets. The ultrathin WO<sub>3</sub> and g-C<sub>3</sub>N<sub>4</sub> nanosheets were obtained by electrostatic-assisted ultrasonic exfoliation of bulk WO<sub>3</sub> and a two-step thermal-etching of bulk g-C<sub>3</sub>N<sub>4</sub>, respectively. The thickness of ultrathin WO<sub>3</sub> and g-C<sub>3</sub>N<sub>4</sub> nanosheets are 2.5–3.5 nm, which is equivalent to 5–8 atomic or molecular layer thickness. This ultrathin layered heterojunction structure can enhance surface photocatalytic rate because photogenerated electrons and holes at heterogeneous interface more easily transfer to surface of photocatalysts. Therefore, the obtained ultrathin 2D/2D WO<sub>3</sub>/g-C<sub>3</sub>N<sub>4</sub> step-scheme (S-scheme) heterojunction photocatalysts exhibited better H<sub>2</sub>-production activity than pure g-C<sub>3</sub>N<sub>4</sub> and WO<sub>3</sub> with the same loading amount of Pt as cocatalyst. The mechanism and driving force of charge transfer and separation in S-scheme heterojunction photocatalysts are investigated and discussed. This investigation will provide new insight about designing and constructing novel S-scheme heterojunction photocatalysts.

## 1. Introduction

Photocatalytic hydrogen (H<sub>2</sub>) generation has been considered as one of the most promising routes to convert solar energy into available chemical energy [1–7]. However, single-semiconductor photocatalysts cannot reach high photocatalytic activity due to their high recombination probability of photogenerated charge carriers and their limited redox potential. Constructing suitable heterojunction systems is an effective way to solve this issue [8–15]. Generally, the design of high efficiency H<sub>2</sub>-generation heterojunction photocatalysts mainly focuses on two key points. One is the suitable band staggered arrangement of two semiconductors, and the other is the ideal interfaces for charge transfer/separation between them [16].

Since Wang et al. firstly used graphitic carbon nitride (g-C<sub>3</sub>N<sub>4</sub>) for H<sub>2</sub> generation by photocatalytic water splitting [17], g-C<sub>3</sub>N<sub>4</sub> attracted much attention due to its narrow bandgap with visible-light response, high conduction band (CB) position with high reduction ability, simple syntheses, and special two-dimensional (2D) layered structure

[5,8,11,18–21]. However, the photocatalytic performance of pure g-C<sub>3</sub>N<sub>4</sub> is still far from the practical requirement [22]. A variety of semiconductors with staggered band structure relative to g-C<sub>3</sub>N<sub>4</sub> have been used to couple with g-C<sub>3</sub>N<sub>4</sub> for constructing g-C<sub>3</sub>N<sub>4</sub>-based heterogeneous photocatalysts, such as TiO<sub>2</sub>/g-C<sub>3</sub>N<sub>4</sub> [18,23–26], ZnO/g-C<sub>3</sub>N<sub>4</sub> [27–30], WO<sub>3</sub>/g-C<sub>3</sub>N<sub>4</sub> [31–35], CdS/g-C<sub>3</sub>N<sub>4</sub> [36–38], ZnIn<sub>2</sub>S<sub>4</sub>/g-C<sub>3</sub>N<sub>4</sub> [39], BiOI/g-C<sub>3</sub>N<sub>4</sub> [40]. At the interfaces of these type-II heterojunctions, the photogenerated electrons will transfer from the semiconductor with higher conduction band (CB) to that with lower CB, while the photogenerated holes will transfer from the semiconductor with lower valence band (VB) to that with higher VB. As shown in Fig. 1a, the interfacial charge transfer in conventional type-II heterojunctions greatly reduces the redox abilities of photogenerated electrons and holes. This kind of charge transfer mechanism thermodynamically is not beneficial for the occurrence of photocatalytic oxidation and reduction reactions [8]. Moreover, the photogenerated electrons in CB of photocatalyst II (PC II) are difficult to transfer to CB of photocatalyst I (PC I) due to their strong Coulomb electrostatic

\* Corresponding author at: State Key Laboratory of Advanced Technology for Material Synthesis and Processing, Wuhan University of Technology, Wuhan, 430070, Hubei, PR China.

E-mail address: [yujiaguo93@whut.edu.cn](mailto:yujiaguo93@whut.edu.cn) (J. Yu).

<https://doi.org/10.1016/j.apcatb.2018.11.011>

Received 28 October 2018; Received in revised form 30 October 2018; Accepted 3 November 2018

Available online 05 November 2018

0926-3373/ © 2018 Elsevier B.V. All rights reserved.

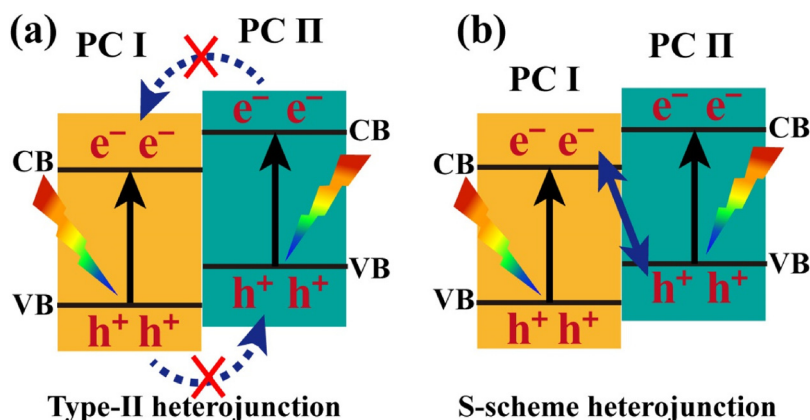


Fig. 1. The schematic diagrams of charge transfer in conventional type-II heterojunction (a) and S-scheme heterojunction (b).

repulsive force [41,42]. Also, the Coulombic attraction force between the electrons (in CB of PC II) and holes (in VB of PC II) also hinders this electron transfer. Similarly, the holes in VB of PC I also cannot easily transfer to VB of PC II. Therefore, the charge transfer mechanism of conventional type-II heterojunction is with obvious limitations from viewpoint of kinetics.

To overcome the shortcomings of conventional type-II heterojunction, meanwhile, to combine our previous work on Z-scheme photocatalyst [41–50], a new step-scheme (S-scheme) heterojunction concept is proposed and illustrated in Fig. 1b. This S-scheme heterojunction photocatalyst is mainly composed of two n-type semiconductor photocatalysts, and PC I and PC II represent oxidation photocatalyst and reduction photocatalyst, respectively. The transfer of photogenerated electrons in S-scheme heterojunction is more like “step” (macroscopic viewpoint) or “N” (microscopic viewpoint) type. The electrons and holes are separated in space, locating in CB of PC II and VB of PC I, respectively. The driving force of charge carrier transfer is mainly from the internal electric field between PC I and PC II. Usually, the oxidation photocatalyst PC I has greater work function and lower Fermi level; contrarily, the reduction photocatalyst PC II has smaller work function and higher Fermi level. When PC I and PC II contact, the electrons in PC II will transfer to PC I across their interface. An internal electric field will be built and its direction is from PC II to PC I. In S-scheme heterojunction, comparatively useless electrons in the CB of PC I and comparatively useless holes in the VB of PC II are recombined and eliminated at the interface. Contrarily, useful holes in VB of PC I and useful electrons in CB of PC II are kept due to the presence of the internal electric field. Finally, photocatalytic oxidation and reduction reactions are initiated by holes in the VB of PC I and electrons in the CB of PC II, respectively.

Herein, ultrathin 2D tungsten trioxide ( $\text{WO}_3$ ) and  $\text{g-C}_3\text{N}_4$  nanosheets are first prepared. Then, 2D/2D  $\text{WO}_3/\text{g-C}_3\text{N}_4$  S-scheme heterogeneous composite photocatalysts are constructed with an electrostatic self-assembly method. The prepared samples are carefully characterized by X-ray diffraction (XRD), transmission electron microscopy (TEM), atomic force microscopy (AFM), X-ray photoelectron spectroscopy (XPS), Raman spectroscopy and Zeta potential measurement, etc. The  $\text{H}_2$ -production performance of the samples is evaluated by water splitting using lactic acid as a sacrificial agent. The S-scheme heterojunction photocatalytic mechanism in 2D/2D  $\text{WO}_3/\text{g-C}_3\text{N}_4$  composites is in depth analyzed and discussed.

## 2. Experimental section

### 2.1. Preparation of bulk $\text{WO}_3$

Firstly, 500 mg of  $\text{Na}_2\text{WO}_4 \cdot 2\text{H}_2\text{O}$  was dissolved in 200 mL of  $\text{HNO}_3$  solution (4.8 M). The mixture solution was stirred for 36 h. Then, the

yellow precipitate ( $\text{WO}_3 \cdot 2\text{H}_2\text{O}$ ) was collected by centrifugation, and washed with water until the neutral pH. The collected  $\text{WO}_3 \cdot 2\text{H}_2\text{O}$  was dried for 12 h. The bulk  $\text{WO}_3$  was obtained by directly calcining the dried  $\text{WO}_3 \cdot 2\text{H}_2\text{O}$  powder with a 5 °C/min heating rate and keeping at 500 °C for 3 h.

### 2.2. Preparation of ultrathin 2D $\text{WO}_3$ nanosheets

The ultrathin  $\text{WO}_3$  nanosheets were obtained by electrostatic-assisted ultrasonic exfoliation of bulk  $\text{WO}_3$ , with bovine serum albumin (BSA) used as an exfoliating agent. The abundant surface  $-\text{NH}_2$  groups of BSA exhibit strong electrostatic binding with  $\text{WO}_3$  under acidic condition. This strong electrostatic force can facilitate the dissociation of  $\text{WO}_3$  nanosheets from the surface of bulk  $\text{WO}_3$ , and greatly improve the dispersity of  $\text{WO}_3$  nanosheets in solution [51]. In a typical experiment, 10 mg of BSA was dissolved in 100 mL of  $\text{H}_2\text{O}$ , and then the pH of the mixture solution was adjusted to 4 with 1 M  $\text{HNO}_3$ . 50 mg of bulk  $\text{WO}_3$  powder was dispersed in the above solution and vigorously sonicated for 3 h. The resulting milky suspension was subjected to centrifugation at 4500 rpm for 30 min. After removing the supernatant BSA solution, the precipitant was re-dispersed in 100 mL of  $\text{H}_2\text{O}$  with pH = 4 and vigorously sonicated for another 1 h. Finally, the white milky  $\text{WO}_3$  suspension was obtained and stored prior to use. The concentration of  $\text{WO}_3$  nanosheets in the suspension was 0.5 mg/mL.

### 2.3. Preparation of ultrathin 2D $\text{g-C}_3\text{N}_4$ nanosheets

$\text{g-C}_3\text{N}_4$  nanosheets were prepared by a two-step calcination thermal-etching method using urea as precursor [50]. The detailed methods are shown in the Supporting information.

### 2.4. Preparation of ultrathin 2D/2D $\text{WO}_3/\text{g-C}_3\text{N}_4$ composite

$\text{WO}_3/\text{g-C}_3\text{N}_4$  composites were prepared by electrostatic self-assembly of  $\text{WO}_3$  nanosheets and  $\text{g-C}_3\text{N}_4$  nanosheets. Their preparation method is provided in the Supporting information.

The detailed methods for characterization, photocatalytic  $\text{H}_2$  generation test and computational calculations are given in the Supporting information.

## 3. Results and discussion

### 3.1. Zeta potential

Fig. 2a exhibits the zeta potentials of bulk  $\text{WO}_3$ ,  $\text{WO}_3$  nanosheets and  $\text{g-C}_3\text{N}_4$  nanosheets at pH = 4. The bulk  $\text{WO}_3$  shows a negative zeta potential of  $-9.7$  mV at pH = 4, whereas the  $\text{WO}_3$  nanosheets exhibit a more negative zeta potential of  $-22.8$  mV at the same pH. The higher

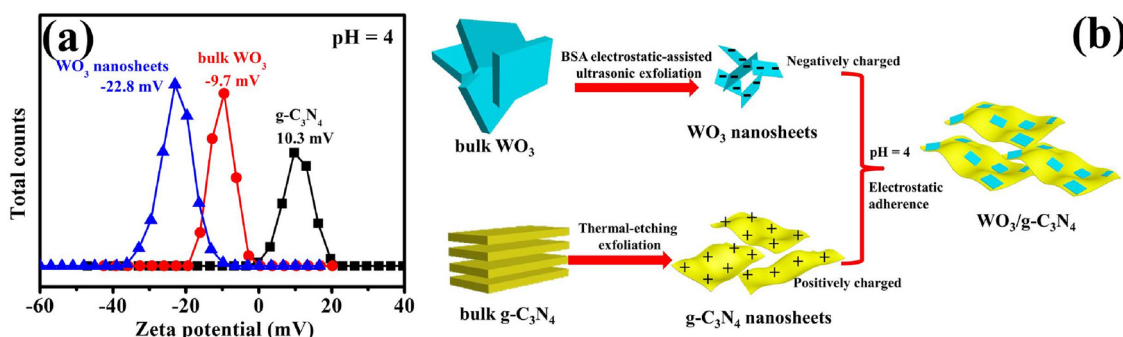


Fig. 2. (a) Zeta potentials of bulk  $\text{WO}_3$ ,  $\text{WO}_3$  nanosheets and  $\text{g-C}_3\text{N}_4$  at pH = 4. (b) The formation schematic diagram of 2D/2D  $\text{WO}_3/\text{g-C}_3\text{N}_4$  heterojunctions by Coulomb electrostatic interaction.

zeta potential value indicates better dispersity of  $\text{WO}_3$  nanosheets than bulk  $\text{WO}_3$ . The exfoliation exposes more surface groups and improves the dispersity of  $\text{WO}_3$  nanosheets. The  $\text{g-C}_3\text{N}_4$  nanosheets exhibit a positive zeta potential of 10.3 mV at pH = 4. The opposite zeta potentials result in strong electrostatic attraction between  $\text{WO}_3$  and  $\text{g-C}_3\text{N}_4$  nanosheets [52], which is beneficial for the charge transfer between them. Thus, stable 2D/2D  $\text{WO}_3/\text{g-C}_3\text{N}_4$  heterojunctions are obtained by the Coulomb electrostatic interaction. The fabrication schematic diagram of the 2D/2D  $\text{WO}_3/\text{g-C}_3\text{N}_4$  heterojunctions is shown in Fig. 2b.

### 3.2. Morphological characteristics

TEM analysis is a powerful tool to study the ultrathin nanosheets. As shown in Fig. 3a, clear nanosheet structure is observed for the  $\text{WO}_3$  nanosheet sample, with the lateral size of  $\text{WO}_3$  nanosheets measured at about  $50 \times 50$  nm. The low contrast of TEM image indicates ultrathin thickness of  $\text{WO}_3$  nanosheets, which is further investigated by AFM (Fig. 4a and b). Clearly, the lateral size of  $\text{WO}_3$  nanosheets is between 50 and 100 nm, and the thickness of  $\text{WO}_3$  nanosheets is 3–4 nm, which directly prove the presence of ultrathin  $\text{WO}_3$  nanosheets (with 5–8 atom or molecular layers). The HRTEM image of  $\text{WO}_3$  nanosheets (corresponding to the part in the red circle in Fig. 3a) is shown in Fig. 3b, and clear lattice fringes are observed. Combined with the electronic diffraction pattern (inset of Fig. 3b), the  $\text{WO}_3$  nanosheets are single crystal nanosheets with good crystallinity. The measured fringe spacings are 0.377 and 0.365 nm, which can be assigned to the (020) and (200) facets of monoclinic  $\text{WO}_3$ , respectively. Fig. 3c presents TEM image of  $\text{g-C}_3\text{N}_4$ . Flexible nanosheets with large lateral size can be observed, which is typical characteristics of  $\text{g-C}_3\text{N}_4$  nanosheets. The HRTEM image (Fig. 3d, corresponding to the part in the red circle in Fig. 3c) indicates that the thickness of  $\text{g-C}_3\text{N}_4$  nanosheets is also very small. The actual thickness of  $\text{g-C}_3\text{N}_4$  nanosheets was also measured by the AFM. As shown in Fig. 4c and 4d, the  $\text{g-C}_3\text{N}_4$  nanosheets show microscale lateral size and the thickness of  $\text{g-C}_3\text{N}_4$  is about 2.5 nm. The interlayer spacing of  $\text{g-C}_3\text{N}_4$  is 0.36 nm, and thus the ultrathin  $\text{g-C}_3\text{N}_4$  nanosheets are about seven molecular layers in thickness. In the TEM image of 15%  $\text{WO}_3/\text{g-C}_3\text{N}_4$  sample (Fig. 3e), the circled parts with higher contrast can be assigned to the  $\text{WO}_3$  nanosheets, whose sizes are consistent with the pure  $\text{WO}_3$  nanosheets shown in Figs. 3a and 4a. For further observation, HRTEM image (Fig. 3f) exhibits the clear contact interface of  $\text{WO}_3$  and  $\text{g-C}_3\text{N}_4$ . Clear lattice fringes in the upper part of the image can be ascribed to  $\text{WO}_3$ . The interfacial contact of  $\text{WO}_3$  and  $\text{g-C}_3\text{N}_4$  is very close, which can be attributed to the strong interfacial electrostatic adherence force. This intimate interfacial contact is beneficial for the interfacial charge transfer between  $\text{WO}_3$  and  $\text{g-C}_3\text{N}_4$ .

### 3.3. Phase structure and surface chemical state

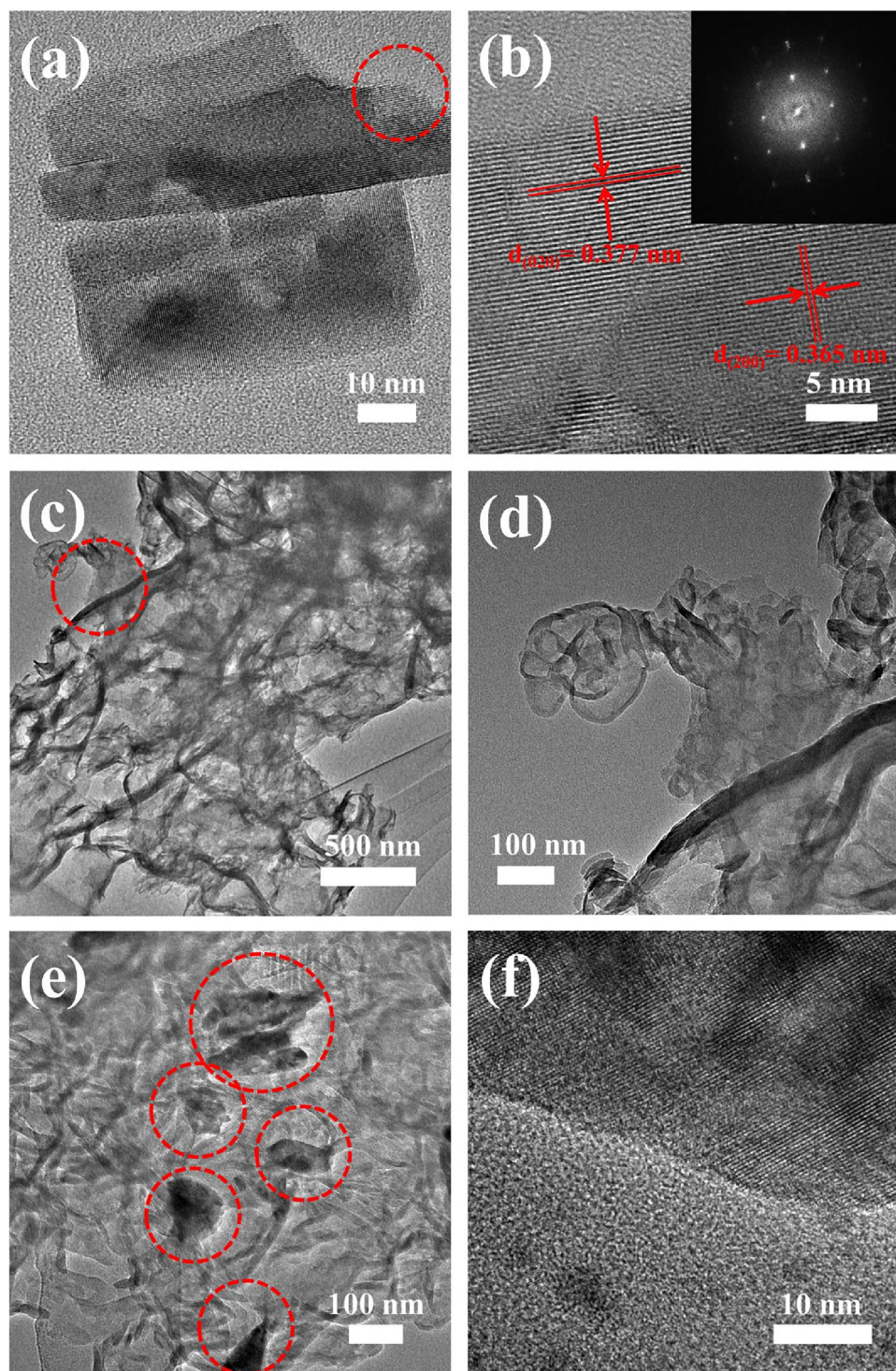
exfoliated  $\text{WO}_3$  nanosheets, bulk  $\text{WO}_3$  and  $\text{WO}_3 \cdot 2\text{H}_2\text{O}$ . All the typical peaks of  $\text{WO}_3 \cdot 2\text{H}_2\text{O}$  sample can be indexed to the corresponding reflections of monoclinic  $\text{WO}_3 \cdot 2\text{H}_2\text{O}$  (JCPDS PDF No. 40–0693). XRD pattern of  $\text{WO}_3$  nanosheets is similar to that of bulk  $\text{WO}_3$ , which means that exfoliation treatment does not change the main crystal structure of  $\text{WO}_3$ . All the peaks are ascribed to the monoclinic  $\text{WO}_3$  (JCPDS PDF No. 83-0950) [53], and no other impurity peak can be observed, implying the high purity of  $\text{WO}_3$  nanosheets products. It is noteworthy that XRD peaks of exfoliated  $\text{WO}_3$  nanosheets become much weaker and broader than that of bulk  $\text{WO}_3$ , which can be ascribed to the thinner nanosheet structure of exfoliated  $\text{WO}_3$  nanosheets. This indicates the successful exfoliation of bulk  $\text{WO}_3$  through the BSA electrostatic-assisted ultrasonic exfoliation method.

Fig. 5a compares XRD patterns of  $\text{g-C}_3\text{N}_4$  nanosheets,  $\text{WO}_3$  nanosheets and  $\text{WO}_3/\text{g-C}_3\text{N}_4$  composites with different  $\text{WO}_3$  percentages. The XRD pattern of pure  $\text{g-C}_3\text{N}_4$  exhibits a typical peak located at  $27.5^\circ$ , ascribed to the characteristic interlayer stacking of aromatic system [22,54,55]. Another characteristic peak located at about  $13^\circ$  (in-plane structural packing motif of tri-s-triazine units) is too weak to be directly observed. Moreover, a clear broad peak located at about  $22^\circ$  can be observed, which is a characteristic peak of amorphous matter. This observation indicates the successful exfoliation of  $\text{g-C}_3\text{N}_4$  during the second thermal treatment, and ultrathin  $\text{g-C}_3\text{N}_4$  nanosheets are obtained [56]. In the case of  $\text{WO}_3/\text{g-C}_3\text{N}_4$  composites, the XRD patterns are seen as the combination of XRD patterns of  $\text{WO}_3$  nanosheets and  $\text{g-C}_3\text{N}_4$  nanosheets. With increasing contents of  $\text{WO}_3$  nanosheets, the XRD peak intensities of  $\text{WO}_3$  become stronger. These results demonstrate the good integration of  $\text{WO}_3$  nanosheets and  $\text{g-C}_3\text{N}_4$  nanosheets in the  $\text{WO}_3/\text{g-C}_3\text{N}_4$  composites.

Fig. 5b compares FTIR spectra of  $\text{g-C}_3\text{N}_4$ , bulk  $\text{WO}_3$ ,  $\text{WO}_3$  nanosheets and 15%  $\text{WO}_3/\text{g-C}_3\text{N}_4$ . No obvious difference is observed in the spectra of bulk  $\text{WO}_3$  and  $\text{WO}_3$  nanosheets, and the broad peak located at  $450\text{--}900\text{ cm}^{-1}$  is assigned to the stretching vibration of W–O–W [57]. As for pure  $\text{g-C}_3\text{N}_4$  nanosheets, the absorption bands located at  $3000\text{--}3500\text{ cm}^{-1}$  are assigned to the amino and surface hydroxyl groups. The bands at  $1200\text{--}1600\text{ cm}^{-1}$  are the characteristic of C–N bonds in the tri-s-triazine units of  $\text{g-C}_3\text{N}_4$ . A sharp band at  $810\text{ cm}^{-1}$  is from the characteristic breathing-vibration of tri-s-triazine units [22,58]. The 15%  $\text{WO}_3/\text{g-C}_3\text{N}_4$  exhibits a similar spectrum with pure  $\text{g-C}_3\text{N}_4$ . Closer examination on the region of  $900\text{--}1100\text{ cm}^{-1}$  (Fig. 5c) reveals a small broad band assigned to  $\text{WO}_3$ . These results indicate successful combination of  $\text{WO}_3$  and  $\text{g-C}_3\text{N}_4$  in the 15%  $\text{WO}_3/\text{g-C}_3\text{N}_4$ .

Fig. 5d shows Raman spectra of  $\text{g-C}_3\text{N}_4$ , bulk  $\text{WO}_3$ ,  $\text{WO}_3$  nanosheets and 15%  $\text{WO}_3/\text{g-C}_3\text{N}_4$ . Firstly, the  $\text{WO}_3$  nanosheets exhibit a similar spectrum to that of its bulk counterpart. The Raman peaks located at  $275$  and  $328\text{ cm}^{-1}$  are ascribed to the bending vibration mode of O–W–O, while those located at  $712$  and  $810\text{ cm}^{-1}$  are due to the stretching vibration mode of W–O [53,59]. It is worth noting that Raman peaks of  $\text{WO}_3$  nanosheets become broader and weaker as compared to bulk  $\text{WO}_3$ , which is due to the phonon softening and





**Fig. 3.** TEM and HRTEM images of (a,b)  $\text{WO}_3$  nanosheets, (c,d)  $\text{g-C}_3\text{N}_4$  nanosheets and (e,f) 15% $\text{WO}_3/\text{g-C}_3\text{N}_4$  samples. (For interpretation of the references to colour in the text, the reader is referred to the web version of this article.)

enhanced electron–phonon coupling in the few-layered region [53]. Raman spectra of  $\text{g-C}_3\text{N}_4$  nanosheets and 15% $\text{WO}_3/\text{g-C}_3\text{N}_4$  show no obvious peaks, which is attributed to the strong interference by fluorescence effect of  $\text{g-C}_3\text{N}_4$ . The enlarged range within the  $750\text{--}900\text{ cm}^{-1}$  range are shown in Fig. 5e, in which two small Raman peaks at  $712$  and  $810\text{ cm}^{-1}$  can be observed for 15% $\text{WO}_3/\text{g-C}_3\text{N}_4$ . This result further confirms successful combination of  $\text{WO}_3$  and  $\text{g-C}_3\text{N}_4$  in 15% $\text{WO}_3/\text{g-C}_3\text{N}_4$ .

### 3.4. XPS analysis

The surface chemical states were further investigated by XPS. All binding energies were calibrated by C 1s binding energy at  $284.8\text{ eV}$ . XPS spectra of bulk  $\text{WO}_3$  and  $\text{WO}_3$  nanosheets are presented in Fig. S2 (Supporting information). As shown in Fig. S2a, compared with bulk  $\text{WO}_3$ , two new C 1s peaks located at  $286.5$  and  $288.0\text{ eV}$  can be observed in the spectrum of  $\text{WO}_3$  nanosheets, which can be assigned to the C–N and –COOH bands of the surface BSA residual. Fig. S2b exhibits

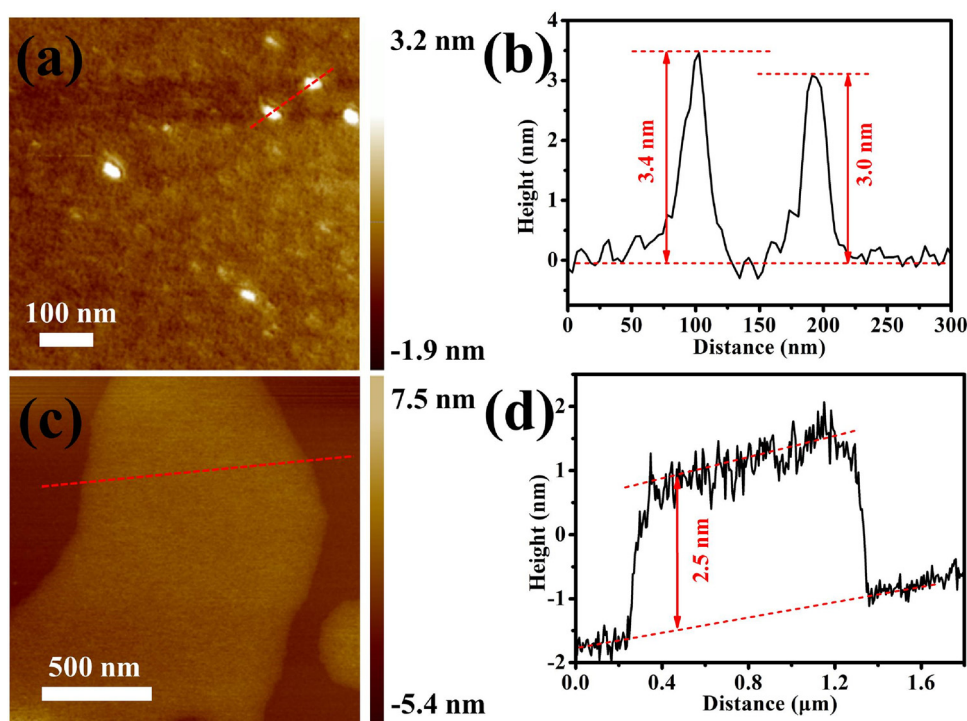


Fig. 4. AFM images of (a,b)  $\text{WO}_3$  nanosheets and (c,d)  $\text{g-C}_3\text{N}_4$  nanosheets.

the comparison of W 4f spectra of bulk  $\text{WO}_3$  and  $\text{WO}_3$  nanosheets. Two peaks at 35.9 and 38.1 eV are ascribed to the W 4f<sub>7/2</sub> and W 4f<sub>5/2</sub> of  $\text{W}^{6+}$ , respectively. A small broad peak at about 41.5 eV is assigned to the W 5p<sub>3/2</sub>. For the  $\text{WO}_3$  nanosheets, another two peaks at 35.0 and 37.2 eV were observed, which can be attributed to the W 4f<sub>7/2</sub> and W 4f<sub>5/2</sub> of  $\text{W}^{5+}$ . The  $\text{W}^{5+}$  is derived from the unsaturated W–O bonds on the surface of  $\text{WO}_3$  nanosheets. The presence of  $\text{W}^{5+}$  indicates

exfoliation of bulk  $\text{WO}_3$  into ultrathin  $\text{WO}_3$  nanosheets. Fig. S2c shows the O 1s spectra of bulk  $\text{WO}_3$  and  $\text{WO}_3$  nanosheets. The peak at 530.5 eV is from the lattice oxygen in bulk  $\text{WO}_3$ . The  $\text{WO}_3$  nanosheets exhibit two peaks at 529.7 and 531.0 eV. The former is assigned to the lattice oxygen at the surface of  $\text{WO}_3$  nanosheets, while the latter is from the surface adsorbed oxygen species.

Fig. 6a exhibits C 1s spectra of  $\text{g-C}_3\text{N}_4$ , 15% $\text{WO}_3/\text{g-C}_3\text{N}_4$  and  $\text{WO}_3$

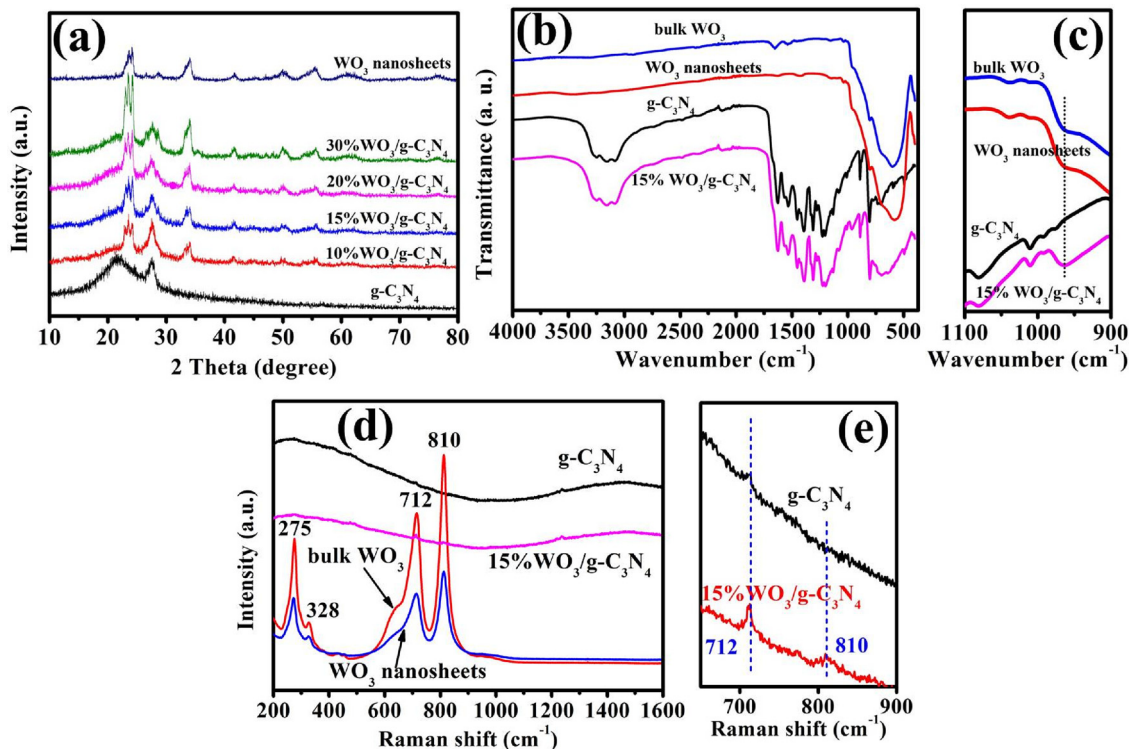


Fig. 5. (a) XRD patterns for  $\text{g-C}_3\text{N}_4$ ,  $\text{WO}_3$  nanosheets and their composites. (b) FTIR and (d) Raman spectra for  $\text{g-C}_3\text{N}_4$ , bulk  $\text{WO}_3$ ,  $\text{WO}_3$  nanosheets and 15% $\text{WO}_3/\text{g-C}_3\text{N}_4$ . (c) and (e) are the enlarged parts of (b) and (d), respectively.



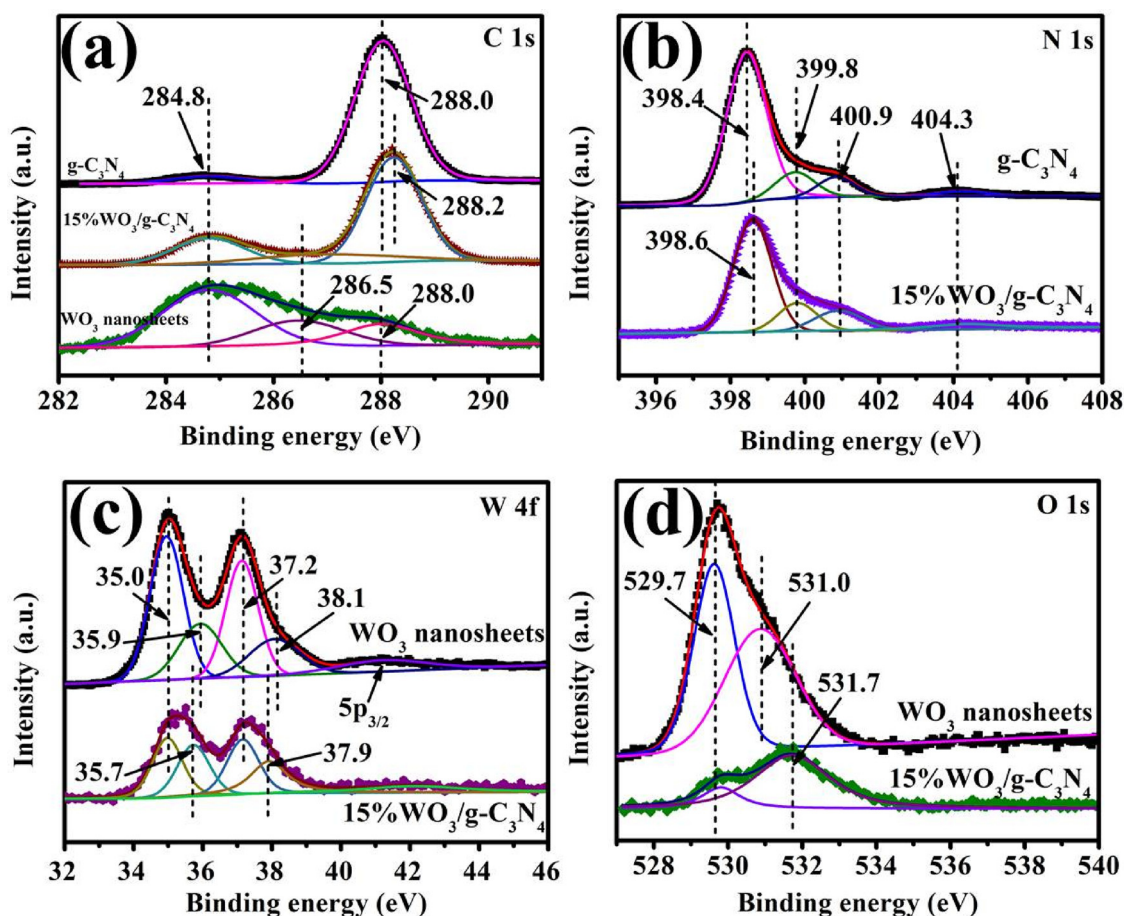


Fig. 6. Comparison of (a) C 1s, (b) N 1s, (c) W 4f and (d) O 1s XPS spectra of g-C<sub>3</sub>N<sub>4</sub>, 15%WO<sub>3</sub>/g-C<sub>3</sub>N<sub>4</sub> and WO<sub>3</sub> nanosheets.

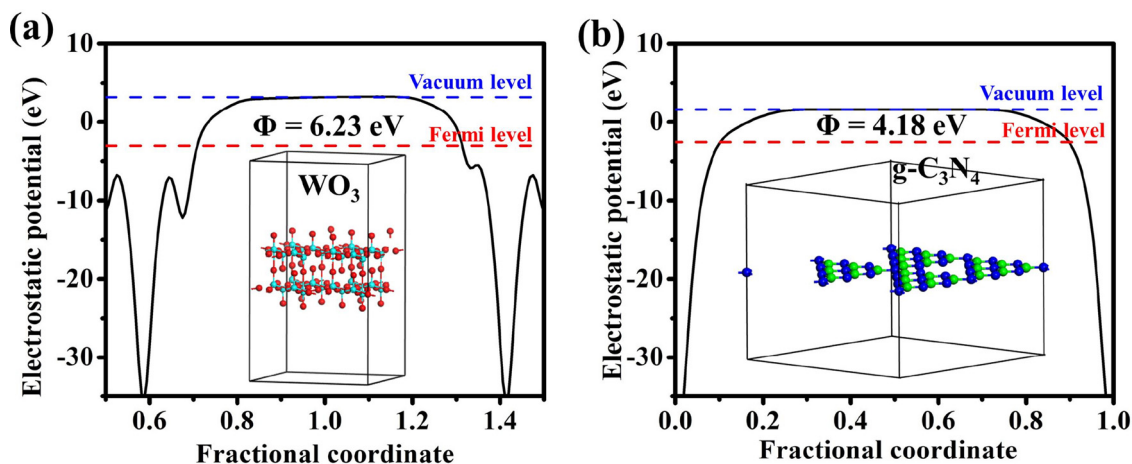


Fig. 7. Electrostatic potentials of (a) WO<sub>3</sub> (001) surface and (b) g-C<sub>3</sub>N<sub>4</sub> (001) surface. Insets show the structural models of the materials for DFT calculation.

nanosheets. The XPS peaks at 288.0 and 288.2 eV of g-C<sub>3</sub>N<sub>4</sub> and 15% WO<sub>3</sub>/g-C<sub>3</sub>N<sub>4</sub> are assigned to the N=C–N<sub>2</sub> bonds of g-C<sub>3</sub>N<sub>4</sub> components [60]. The slight positive shift of C 1s peak (by 0.2 eV) is caused by the charge transfer at the interface of g-C<sub>3</sub>N<sub>4</sub> and WO<sub>3</sub>. The N 1s spectra of g-C<sub>3</sub>N<sub>4</sub> and 15%WO<sub>3</sub>/g-C<sub>3</sub>N<sub>4</sub> are shown in Fig. 6b. The peak at 399.8 eV is assigned to three-coordinate N(C<sub>3</sub>), the peak at 400.9 eV to the surface amino group (–NH<sub>2</sub>), the peak at 404.3 eV to the  $\pi$ -excitation of C–N heterocycles, and the peaks at 398.4 and 398.6 eV to the two-coordinate N species (C = N–C) [22,60]. The slight positive shift of N 1s peak (by 0.2 eV) is also attributed to the interfacial charge transfer of g-C<sub>3</sub>N<sub>4</sub> and WO<sub>3</sub>. To further investigate the charge transfer

between g-C<sub>3</sub>N<sub>4</sub> and WO<sub>3</sub> in 15%WO<sub>3</sub>/g-C<sub>3</sub>N<sub>4</sub>, the comparison of W 4f spectra of WO<sub>3</sub> nanosheets and 15%WO<sub>3</sub>/g-C<sub>3</sub>N<sub>4</sub> is presented in Fig. 6c. The binding energies of W<sup>6+</sup> at 35.9 and 38.1 eV in WO<sub>3</sub> nanosheets negatively shift to 35.7 and 37.9 eV in 15%WO<sub>3</sub>/g-C<sub>3</sub>N<sub>4</sub>. The positive shifts of C 1s and N 1s, and the negative shift of W<sup>6+</sup> indicate the charge transfer from g-C<sub>3</sub>N<sub>4</sub> to WO<sub>3</sub> at the interfaces [60]. It is noted that, in the O 1s spectra of WO<sub>3</sub> nanosheets and 15%WO<sub>3</sub>/g-C<sub>3</sub>N<sub>4</sub> (Fig. 6d), the binding energy of lattice oxygen at 529.7 eV shows no obvious shift, while that of the surface adsorbed oxygen species positively shifts from the 531.0 eV of WO<sub>3</sub> nanosheets to 531.7 eV of 15% WO<sub>3</sub>/g-C<sub>3</sub>N<sub>4</sub>, which is ascribed to the oxidation of adsorbed BSA during

irradiation.

### 3.5. Density functional theory computational calculations

Density functional theory (DFT) computational calculations were used to further investigate the interfacial charge transfer between  $\text{WO}_3$  and  $\text{g-C}_3\text{N}_4$  [61]. As shown in Fig. S3 (Supporting information), the calculated band gap energies of  $\text{WO}_3$  and  $\text{g-C}_3\text{N}_4$  are 2.77 and 2.68 eV, respectively. Fig. 7 exhibits the electrostatic potentials of  $\text{WO}_3$  (001) surface and  $\text{g-C}_3\text{N}_4$  (001) surface. The work functions of  $\text{WO}_3$  (001) surface and  $\text{g-C}_3\text{N}_4$  (001) surface are calculated to be 6.23 and 4.18 eV, respectively. The difference of work function indicates the presence of charge transfer at the interface of  $\text{WO}_3$  and  $\text{g-C}_3\text{N}_4$ . The greater work function of  $\text{WO}_3$  will lead to the charge transfer from  $\text{g-C}_3\text{N}_4$  to  $\text{WO}_3$  until the Fermi level equilibrium. This charge transfer will result in the production of interfacial built-in electric field. At the interface, the surface of  $\text{g-C}_3\text{N}_4$  is positively charged, while the surface of  $\text{WO}_3$  is negatively charged. This result is consistent with the charge transfer from  $\text{g-C}_3\text{N}_4$  to  $\text{WO}_3$  as revealed by XPS results. Due to the thin layered structures of  $\text{g-C}_3\text{N}_4$  and  $\text{WO}_3$  and their strong Coulomb force, the intensity of built-in electric field is greatly enhanced, which is more beneficial for the transfer and separation of interfacial charge carriers than their bulk counterparts.

### 3.6. Photocatalytic hydrogen generation

Fig. 8a exhibits comparison of photocatalytic  $\text{H}_2$ -generation rates of the as-prepared samples using lactic acid as a hole-sacrificial agent.  $\text{WO}_3$  nanosheets have no obvious  $\text{H}_2$  generation activity observed due to their low CB position. Pure  $\text{g-C}_3\text{N}_4$  nanosheets show obvious  $\text{H}_2$ -generation activity due to their high CB position and photogenerated electrons with enough reduction ability. In the presence of a small amount of  $\text{WO}_3$  nanosheets, the  $\text{H}_2$ -production activity of  $\text{WO}_3/\text{g-C}_3\text{N}_4$  composite is obviously enhanced. Especially, the 15% $\text{WO}_3/\text{g-C}_3\text{N}_4$  composite sample exhibits the highest  $\text{H}_2$ -production activity (982  $\mu\text{mol}/\text{h}/\text{g}$ ), and its activity is about 1.7 times higher than pure  $\text{g-C}_3\text{N}_4$  nanosheets. Fig. 8b shows that the 15% $\text{WO}_3/\text{g-C}_3\text{N}_4$  sample exhibits good photocatalytic  $\text{H}_2$ -production stability, with no obvious hydrogen activity decrease observed after four cycles.

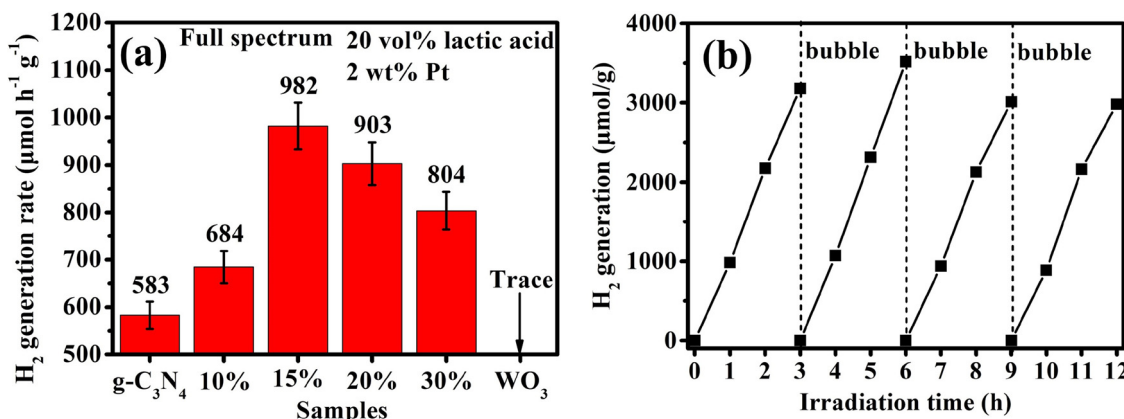
### 3.7. Photocatalytic mechanism

Fig. 9a exhibits the Mott-Schottky plots of  $\text{g-C}_3\text{N}_4$  and  $\text{WO}_3$  nanosheets. Firstly, both  $\text{g-C}_3\text{N}_4$  and  $\text{WO}_3$  nanosheets show positive slopes, indicating the n-type semiconductor characteristic of  $\text{g-C}_3\text{N}_4$  and  $\text{WO}_3$  nanosheets. The flat band position of n-type semiconductors is

closer to their CB position. Thus, the extrapolated CB positions of  $\text{g-C}_3\text{N}_4$  and  $\text{WO}_3$  nanosheets are  $-1.25$  and  $-0.34$  V, respectively (vs  $\text{Ag}/\text{AgCl}$ ,  $\text{pH} = 7$ ). These two potentials are converted to  $-0.61$  and  $+0.30$  V (vs NHE,  $\text{pH} = 0$ ). Combined with the bandgap of  $\text{g-C}_3\text{N}_4$  (2.75 eV) and  $\text{WO}_3$  (2.68 eV) nanosheets, their band structures are shown in Fig. 9b.

Fig. 9c shows electron paramagnetic resonance (EPR) spectra of  $\text{DMPO}\cdot\text{OH}$  measured in aqueous suspensions of the materials. The  $\text{DMPO}\cdot\text{OH}$  signal of  $\text{WO}_3$  nanosheets and 15% $\text{WO}_3/\text{g-C}_3\text{N}_4$  can be observed, while no obvious  $\text{DMPO}\cdot\text{OH}$  signal is observed for pure  $\text{g-C}_3\text{N}_4$ . The absence of  $\text{DMPO}\cdot\text{OH}$  signal in  $\text{g-C}_3\text{N}_4$  is due to the weak oxidation potential of photogenerated holes in  $\text{g-C}_3\text{N}_4$  (2.14 V, vs NHE at  $\text{pH} = 0$ ). The observation of  $\text{DMPO}\cdot\text{OH}$  signal in the 15% $\text{WO}_3/\text{g-C}_3\text{N}_4$  composite suggests that the photogenerated holes still stay in the VB of  $\text{WO}_3$  and do not transfer to the VB of  $\text{g-C}_3\text{N}_4$ . In Fig. 9d, strong  $\text{DMPO}\cdot\text{O}_2^-$  signals are observed for  $\text{g-C}_3\text{N}_4$  and 15% $\text{WO}_3/\text{g-C}_3\text{N}_4$  composite samples in methanolic suspension, whereas very weak  $\text{DMPO}\cdot\text{O}_2^-$  signal is observed for  $\text{WO}_3$  nanosheets. The results indicate that the photogenerated electrons in  $\text{g-C}_3\text{N}_4$  and 15% $\text{WO}_3/\text{g-C}_3\text{N}_4$  composite samples have enough reduction ability to reduce  $\text{O}_2$  to form superoxide radical anions ( $\text{O}_2^-$ ). The above EPR results indicate that the photogenerated electrons and holes respectively are present in the CB of  $\text{g-C}_3\text{N}_4$  and VB of  $\text{WO}_3$ , and the charge transfer does not follow the conventional type II heterojunction mechanism. Contrarily, the above suggested S-scheme heterojunction mechanism can better explain the enhancement of photocatalytic  $\text{H}_2$ -production activity in the 2D/2D  $\text{WO}_3/\text{g-C}_3\text{N}_4$  composite photocatalysts.

Fig. 10 shows charge transfer mechanism of S-scheme heterojunction between  $\text{WO}_3$  and  $\text{g-C}_3\text{N}_4$ . Usually,  $\text{g-C}_3\text{N}_4$  is a reduction-type photocatalyst with smaller work function (4.18 eV) and higher Fermi level. Contrarily,  $\text{WO}_3$  is an oxidation-type photocatalyst with larger work function (6.23 eV) and lower Fermi level (Fig. 10a). When  $\text{g-C}_3\text{N}_4$  and  $\text{WO}_3$  are in close contact, the electrons in  $\text{g-C}_3\text{N}_4$  spontaneously transfer to  $\text{WO}_3$  across their interface until their Fermi levels are the same (Fig. 10b). Thus,  $\text{g-C}_3\text{N}_4$  loses electrons and is positively charged, while the  $\text{WO}_3$  get electrons and is negatively charged at the interface. Naturally, an internal electric field is produced at the interface. Simultaneously, band edge of  $\text{g-C}_3\text{N}_4$  bends upward due to the loss of electrons, but band edge of  $\text{WO}_3$  bends downward due to the accumulation of electrons. Under light irradiation, the electrons are excited from VB to CB of both  $\text{WO}_3$  and  $\text{g-C}_3\text{N}_4$ . The internal electric field, band edge bending and Coulomb interaction accelerate the recombination of some electrons (from CB of  $\text{WO}_3$ ) and holes (from VB of  $\text{g-C}_3\text{N}_4$ ), and, at the same time, prevent the recombination of some electrons (from CB of  $\text{g-C}_3\text{N}_4$ ) and holes (from VB of  $\text{WO}_3$ ) (Fig. 10c). This S-scheme heterojunction mechanism will eliminate the relatively useless electrons



**Fig. 8.** (a) Comparison of  $\text{H}_2$ -generation activities of as-prepared samples under xenon lamp irradiation (full spectrum), with photo-deposition of 2% Pt as cocatalyst (The symbols 10%, 15%, 20% and 30% on the x-axis represent the 10% $\text{WO}_3/\text{g-C}_3\text{N}_4$ , 15% $\text{WO}_3/\text{g-C}_3\text{N}_4$ , 20% $\text{WO}_3/\text{g-C}_3\text{N}_4$  and 30% $\text{WO}_3/\text{g-C}_3\text{N}_4$  samples, respectively). (b) Time courses of photocatalytic  $\text{H}_2$ -generation of 15% $\text{WO}_3/\text{g-C}_3\text{N}_4$ .

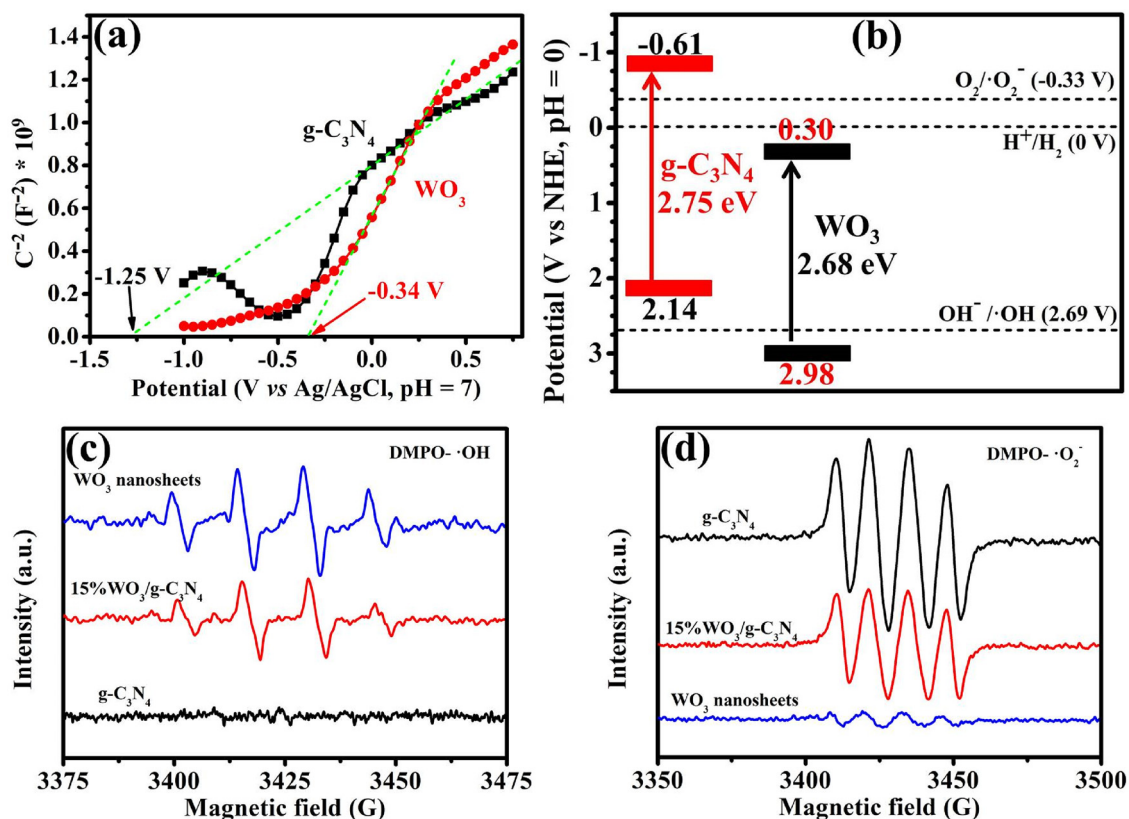


Fig. 9. (a) Mott-Schottky plots and (b) band structures of  $g-C_3N_4$  and  $WO_3$  nanosheets. EPR spectra of (c)  $DMPO \cdot OH$  in aqueous and (d)  $DMPO \cdot O_2^-$  in methanol dispersion in the presence of  $g-C_3N_4$ ,  $WO_3$  nanosheets and 15%  $WO_3/g-C_3N_4$ .

(from CB of  $WO_3$ ) and holes (from VB of  $g-C_3N_4$ ), but hold the useful electrons (from CB of  $g-C_3N_4$ ) and holes (from VB of  $WO_3$ ). This charge carrier transfer process endows the 2D/2D  $WO_3/g-C_3N_4$  composite heterojunction with supreme redox capacity, thus providing strong driving force for running photocatalytic water splitting reaction.

#### 4. Conclusions

In summary, ultrathin 2D/2D  $WO_3/g-C_3N_4$  S-scheme heterojunction photocatalysts were successfully prepared by an electrostatic self-assembly method using ultrathin  $WO_3$  and  $g-C_3N_4$  nanosheets as precursors. The  $H_2$ -production activity of the  $WO_3/g-C_3N_4$  composite

samples was greatly enhanced, which is about 1.7 times higher than pure  $g-C_3N_4$ . The enhanced photocatalytic performance is due to the formation of step-scheme heterojunction, which inhibits the recombination of useful electrons and holes, but expedites the recombination of relatively useless electrons and holes. XPS, work function and EPR results further confirm the presence of step heterojunction mechanism and its correctness. This work will provide new insight for design and fabrication of novel heterojunction photocatalyst. The prepared ultrathin 2D/2D  $WO_3/g-C_3N_4$  composite can also find potential application in electrocatalysis, catalysis, solar cell and adsorption.

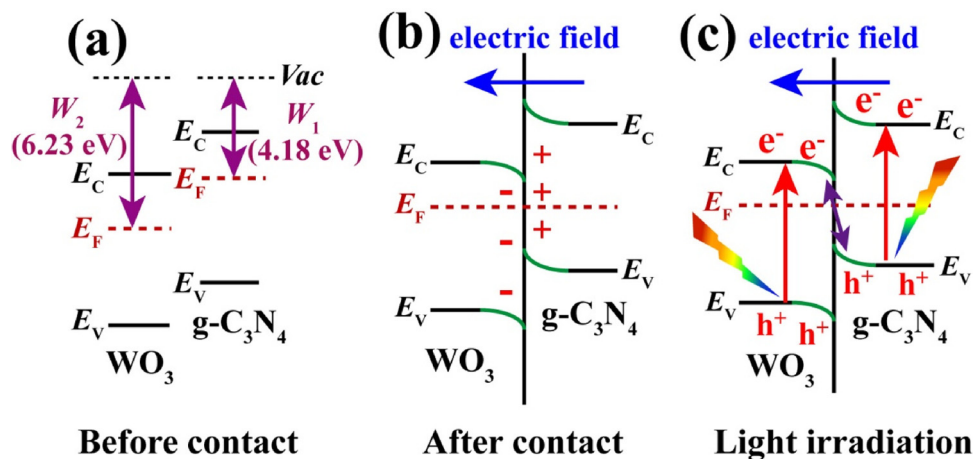


Fig. 10. (a) The work functions of  $g-C_3N_4$  and  $WO_3$  before contact. (b) The internal electric field and band edge bending at the interface of  $WO_3/g-C_3N_4$  after contact. (c) The S-scheme charge transfer mechanism between  $WO_3$  and  $g-C_3N_4$  under light irradiation.



## Acknowledgments

This work was supported by National Natural Science Foundation of China (21433007, 21573170, U1705251 and 51320105001) and Innovative Research Funds of SKLWUT (2017-ZD-4).

## Appendix A. Supplementary data

Supplementary material related to this article can be found, in the online version, at doi:<https://doi.org/10.1016/j.apcatb.2018.11.011>.

## References

- [1] W.J. Ong, L.L. Tan, Y.H. Ng, S.T. Yong, S.P. Chai, Graphitic carbon nitride (g-C<sub>3</sub>N<sub>4</sub>)-based photocatalysts for artificial photosynthesis and environmental remediation: are we a step closer to achieving sustainability? *Chem. Rev.* 116 (2016) 7159–7329.
- [2] J. Fu, B. Zhu, W. You, M. Jaroniec, J. Yu, A flexible bio-inspired H<sub>2</sub>-production photocatalyst, *Appl. Catal. B* 220 (2018) 148–160.
- [3] J. Jiang, S. Cao, C. Hu, C. Chen, A comparison study of alkali metal-doped g-C<sub>3</sub>N<sub>4</sub> for visible-light photocatalytic hydrogen evolution, *Chin. J. Catal.* 38 (2017) 1981–1989.
- [4] L. Bi, X. Gao, Z. Ma, L. Zhang, D. Wang, T. Xie, Enhanced separation efficiency of PtNi<sub>x</sub>/g-C<sub>3</sub>N<sub>4</sub> for photocatalytic hydrogen production, *ChemCatChem* 9 (2017) 3779–3785.
- [5] G. Zhang, Z. Lan, X. Wang, Conjugated polymers: catalysts for photocatalytic hydrogen evolution, *Angew. Chem. Int. Ed.* 55 (2016) 15712–15727.
- [6] D. Ruan, S. Kim, M. Fujitsuka, T. Majima, Defects rich g-C<sub>3</sub>N<sub>4</sub> with mesoporous structure for efficient photocatalytic H<sub>2</sub> production under visible light irradiation, *Appl. Catal. B* 238 (2018) 638–646.
- [7] E.S. Da Silva, N.M.M. Moura, M.G.P.M.S. Neves, A. Coutinho, M. Prieto, C.G. Silva, J.L. Faria, Novel hybrids of graphitic carbon nitride sensitized with free-base meso-tetrakis(carboxyphenyl) porphyrins for efficient visible light photocatalytic hydrogen production, *Appl. Catal. B* 221 (2018) 56–69.
- [8] J. Fu, J. Yu, C. Jiang, B. Cheng, g-C<sub>3</sub>N<sub>4</sub>-based heterostructured photocatalysts, *Adv. Energy Mater.* 8 (2018) 1701503.
- [9] R. Boppella, C.H. Choi, J. Moon, D.H. Kim, Spatial charge separation on strongly coupled 2D-hybrid of rGO/La<sub>2</sub>Ti<sub>2</sub>O<sub>7</sub>/NiFe-LDH heterostructures for highly efficient noble metal free photocatalytic hydrogen generation, *Appl. Catal. B* 239 (2018) 178–186.
- [10] S.A. Rawool, M.R. Pai, A.M. Banerjee, A. Arya, R.S. Ningthoujam, R. Tewari, R. Rao, B. Chalke, P. Ayyub, A.K. Tripathi, S.R. Bhargava, *pn* heterojunctions in NiO:TiO<sub>2</sub> composites with type-II band alignment assisting sunlight driven photocatalytic H<sub>2</sub> generation, *Appl. Catal. B* 221 (2018) 443–458.
- [11] J. Xu, J. Gao, Y. Qi, C. Wang, L. Wang, Anchoring Ni<sub>2</sub>P on the UiO-66-NH<sub>2</sub>/g-C<sub>3</sub>N<sub>4</sub>-derived C-doped ZrO<sub>2</sub>/g-C<sub>3</sub>N<sub>4</sub> heterostructure: highly efficient photocatalysts for H<sub>2</sub> production from water splitting, *ChemCatChem* 10 (2018) 3327–3335.
- [12] Y.H. Hafeez, S.K. Lakhera, P. Karthik, M. Anpo, B. Neppolian, Facile construction of ternary CuFe<sub>2</sub>O<sub>4</sub>-TiO<sub>2</sub> nanocomposite supported reduced graphene oxide (rGO) photocatalysts for the efficient hydrogen production, *Appl. Surf. Sci.* 449 (2018) 772–779.
- [13] S.K. Lakhera, Y.H. Hafeez, P. Veluswamy, V. Ganesh, A. Khan, H. Ikeda, B. Neppolian, Enhanced photocatalytic degradation and hydrogen production activity of in situ grown TiO<sub>2</sub> coupled NiTiO<sub>3</sub> nanocomposites, *Appl. Surf. Sci.* 449 (2018) 790–798.
- [14] W. Yu, S. Zhang, J. Chen, P. Xia, M.H. Richter, L. Chen, W. Xu, J. Jin, S. Chen, T. Peng, Biomimetic Z-scheme photocatalyst with a tandem solid-state electron flow catalyzing H<sub>2</sub> evolution, *J. Mater. Chem. A* 6 (2018) 15668–15674.
- [15] W. Yu, J. Chen, T. Shang, L. Chen, L. Gu, T. Peng, Direct Z-scheme g-C<sub>3</sub>N<sub>4</sub>/WO<sub>3</sub> photocatalyst with atomically defined junction for H<sub>2</sub> production, *Appl. Catal. B* 219 (2017) 693–704.
- [16] C. Wang, D. Qin, D. Shan, J. Gu, Y. Yan, J. Chen, Q. Wang, C. He, Y. Li, J. Quan, X. Lu, Assembly of g-C<sub>3</sub>N<sub>4</sub>-based type II and Z-scheme heterojunction anodes with improved charge separation for photoelectrochemical water oxidation, *Phys. Chem. Chem. Phys.* 19 (2017) 4507–4515.
- [17] X. Wang, K. Maeda, A. Thomas, K. Takanabe, G. Xin, J.M. Carlsson, K. Domen, M. Antonietti, A metal-free polymeric photocatalyst for hydrogen production from water under visible light, *Nat. Mater.* 8 (2009) 76–80.
- [18] M. Wu, J. Zhang, C. Liu, Y. Gong, R. Wang, B. He, H. Wang, Rational design and fabrication of noble-metal-free Ni<sub>2</sub>P cocatalyst embedded 3D N-TiO<sub>2</sub>/g-C<sub>3</sub>N<sub>4</sub> heterojunctions with enhanced photocatalytic hydrogen evolution, *ChemCatChem* 10 (2018) 3069–3077.
- [19] J. Wen, J. Xie, X. Chen, X. Li, A review on g-C<sub>3</sub>N<sub>4</sub>-based photocatalysts, *Appl. Surf. Sci.* 391 (2017) 72–123.
- [20] B. Zhu, L. Zhang, B. Cheng, J. Yu, First-principle calculation study of tri-s-triazine-based g-C<sub>3</sub>N<sub>4</sub>: a review, *Appl. Catal. B* 224 (2018) 983–999.
- [21] F. Chen, H. Yang, W. Luo, P. Wang, H. Yu, Selective adsorption of thiocyanate anions on Ag-modified g-C<sub>3</sub>N<sub>4</sub> for enhanced photocatalytic hydrogen evolution, *Chin. J. Catal.* 38 (2017) 1990–1998.
- [22] J. Fu, B. Zhu, C. Jiang, B. Cheng, W. You, J. Yu, Hierarchical porous O-doped g-C<sub>3</sub>N<sub>4</sub> with enhanced photocatalytic CO<sub>2</sub> reduction activity, *Small* 13 (2017) 1603938.
- [23] K. Wei, K.X. Lie, L.S. Yan, S.L. Luo, H.Q. Guo, Y.H. Dai, X.B. Luo, One-step fabrication of g-C<sub>3</sub>N<sub>4</sub> nanosheets/TiO<sub>2</sub> hollow microspheres heterojunctions with atomic level hybridization and their application in the multi-component synergistic photocatalytic systems, *Appl. Catal. B* 222 (2018) 88–98.
- [24] X. Wei, H. Wang, X. Wang, W. Jiang, Facile fabrication of mesoporous g-C<sub>3</sub>N<sub>4</sub>/TiO<sub>2</sub> photocatalyst for efficient degradation of DNBP under visible light irradiation, *Appl. Surf. Sci.* 426 (2017) 1271–1280.
- [25] J. Li, M. Zhang, Q.Y. Li, J.J. Yang, Enhanced visible light activity on direct contact Z-scheme g-C<sub>3</sub>N<sub>4</sub>-TiO<sub>2</sub> photocatalyst, *Appl. Surf. Sci.* 391 (2017) 184–193.
- [26] Y. Zou, J.-W. Shi, D. Ma, Z. Fan, C. Niu, L. Wang, Fabrication of g-C<sub>3</sub>N<sub>4</sub>/Au/C-TiO<sub>2</sub> hollow structures as visible-light-driven Z-scheme photocatalysts with enhanced photocatalytic H<sub>2</sub> evolution, *ChemCatChem* 9 (2017) 3752–3761.
- [27] S.K. Le, T.S. Jiang, Y.W. Li, Q. Zhao, Y.Y. Li, W.B. Fang, M. Gong, Highly efficient visible-light-driven mesoporous graphitic carbon nitride/ZnO nanocomposite photocatalysts, *Appl. Catal. B* 200 (2017) 601–610.
- [28] H. Jung, P. Thanh-Truc, E.W. Shin, Interactions between ZnO nanoparticles and amorphous g-C<sub>3</sub>N<sub>4</sub> nanosheets in thermal formation of g-C<sub>3</sub>N<sub>4</sub>/ZnO composite materials: the annealing temperature effect, *Appl. Surf. Sci.* 458 (2018) 369–381.
- [29] J. Zhai, T. Wang, C. Wang, D. Liu, UV-light-assisted ethanol sensing characteristics of g-C<sub>3</sub>N<sub>4</sub>/ZnO composites at room temperature, *Appl. Surf. Sci.* 441 (2018) 317–323.
- [30] W. Yu, D. Xu, T. Peng, Enhanced photocatalytic activity of g-C<sub>3</sub>N<sub>4</sub> for selective CO<sub>2</sub> reduction to CH<sub>3</sub>OH via facile coupling of ZnO: a direct Z-scheme mechanism, *J. Mater. Chem. A* 3 (2015) 19936–19947.
- [31] Z. Lou, C. Xue, In situ growth of WO<sub>3-x</sub> nanowires on g-C<sub>3</sub>N<sub>4</sub> nanosheets: 1D/2D heterostructures with enhanced photocatalytic activity, *CrystEngComm* 18 (2016) 8406–8410.
- [32] L. Cui, X. Ding, Y. Wang, H. Shi, L. Huang, Y. Zuo, S. Kang, Facile preparation of Z-scheme WO<sub>3</sub>/g-C<sub>3</sub>N<sub>4</sub> composite photocatalyst with enhanced photocatalytic performance under visible light, *Appl. Surf. Sci.* 391 (2017) 202–210.
- [33] R. Zhao, X. Li, J. Su, X. Gao, Preparation of WO<sub>3</sub>/g-C<sub>3</sub>N<sub>4</sub> composites and their application in oxidative desulfurization, *Appl. Surf. Sci.* 392 (2017) 810–816.
- [34] P. Wang, N. Lu, Y. Su, N. Liu, H. Yu, J. Li, Y. Fang, Fabrication of WO<sub>3</sub>/g-C<sub>3</sub>N<sub>4</sub> with core@shell nanostructure for enhanced photocatalytic degradation activity under visible light, *Appl. Surf. Sci.* 423 (2017) 197–204.
- [35] K. He, J. Xie, X. Luo, J. Wen, S. Ma, X. Li, Y. Fang, X. Zhang, Enhanced visible light photocatalytic H<sub>2</sub> production over Z-scheme g-C<sub>3</sub>N<sub>4</sub> nanosheets/WO<sub>3</sub> nanorods nanocomposites loaded with Ni(OH)<sub>2</sub> cocatalysts, *Chin. J. Catal.* 38 (2017) 240–252.
- [36] J. He, L. Chen, Z.Q. Yi, D. Ding, C.T. Au, S.F. Yin, Fabrication of two-dimensional porous CdS nanoplates decorated with C<sub>3</sub>N<sub>4</sub> nanosheets for highly efficient photocatalytic hydrogen production from water splitting, *Catal. Commun.* 99 (2017) 79–82.
- [37] C. Yin, L. Cui, T. Pu, X. Fang, H. Shi, S. Kang, X. Zhang, Facile fabrication of nano-sized hollow-CdS@g-C<sub>3</sub>N<sub>4</sub> core-shell spheres for efficient visible-light-driven hydrogen evolution, *Appl. Surf. Sci.* 456 (2018) 464–472.
- [38] T.F. Wu, P.F. Wang, J. Qian, Y.H. Ao, C. Wang, J. Hou, Noble-metal-free nickel phosphide modified CdS/C<sub>3</sub>N<sub>4</sub> nanorods for dramatically enhanced photocatalytic hydrogen evolution under visible light irradiation, *Dalton Trans.* 46 (2017) 13793–13801.
- [39] N. Ding, L.S. Zhang, H.Y. Zhang, J.J. Shi, H.J. Wu, Y.H. Luo, D.M. Li, Q.B. Meng, Microwave-assisted synthesis of ZnIn<sub>2</sub>S<sub>4</sub>/g-C<sub>3</sub>N<sub>4</sub> heterojunction photocatalysts for efficient visible light photocatalytic hydrogen evolution, *Catal. Commun.* 100 (2017) 173–177.
- [40] K. Dai, L.H. Lu, C.H. Liang, G. Zhu, Q.Z. Liu, L. Geng, J.Q. He, A high efficient graphitic-C<sub>3</sub>N<sub>4</sub>/BiOI/graphene oxide ternary nanocomposite heterostructured photocatalyst with graphene oxide as electron transport buffer material, *Dalton Trans.* 44 (2015) 7903–7910.
- [41] J. Low, J. Yu, M. Jaroniec, S. Wageh, A.A. Al-Ghamdi, Heterojunction photocatalysts, *Adv. Mater.* 29 (2017) 1601694.
- [42] Q. Xu, L. Zhang, J. Yu, S. Wageh, A.A. Al-Ghamdi, M. Jaroniec, Direct Z-scheme photocatalysts: principles, synthesis, and applications, *Mater. Today* (2018), <https://doi.org/10.1016/j.mat.2018.1004.1008>.
- [43] J. Yu, S. Wang, J. Low, W. Xiao, Enhanced photocatalytic performance of direct Z-scheme g-C<sub>3</sub>N<sub>4</sub>-TiO<sub>2</sub> photocatalysts for the decomposition of formaldehyde in air, *Phys. Chem. Chem. Phys.* 15 (2013) 16883–16890.
- [44] J. Low, C. Jiang, B. Cheng, S. Wageh, A.A. Al-Ghamdi, J. Yu, A review of direct Z-scheme photocatalysts, *Small Methods* 1 (2017) 1700080.
- [45] T. Di, B. Zhu, B. Cheng, J. Yu, J. Xu, A direct Z-scheme g-C<sub>3</sub>N<sub>4</sub>/SnS<sub>2</sub> photocatalyst with superior visible-light CO<sub>2</sub> reduction performance, *J. Catal.* 352 (2017) 532–541.
- [46] J. Low, B. Dai, T. Tong, C. Jiang, J. Yu, In situ irradiated X-ray photoelectron spectroscopy investigation on a direct Z-scheme TiO<sub>2</sub>/CdS composite film photocatalyst, *Adv. Mater.* (2018) 1802981.
- [47] J. Jin, J.G. Yu, D.P. Guo, C. Cui, W.K. Ho, A hierarchical Z-scheme CdS-WO<sub>3</sub> photocatalyst with enhanced CO<sub>2</sub> reduction activity, *Small* 11 (2015) 5262–5271.
- [48] K. Qi, B. Cheng, J. Yu, W. Ho, A review on TiO<sub>2</sub>-based Z-scheme photocatalysts, *Chin. J. Catal.* 38 (2017) 1936–1955.
- [49] P. Zhou, J. Yu, M. Jaroniec, All-solid-state Z-scheme photocatalytic systems, *Adv. Mater.* 26 (2014) 4920–4935.
- [50] Q. Xu, B. Zhu, C. Jiang, B. Cheng, J. Yu, Constructing 2D/2D Fe<sub>2</sub>O<sub>3</sub>/g-C<sub>3</sub>N<sub>4</sub> direct Z-scheme photocatalysts with enhanced H<sub>2</sub> generation performance, *Sol. RRL* 2 (2018) 1800006.
- [51] G. Guan, J. Xia, S. Liu, Y. Cheng, S. Bai, S.Y. Tee, Y.-W. Zhang, M.-Y. Han, Electrostatic-driven exfoliation and hybridization of 2D nanomaterials, *Adv. Mater.* 29 (2017) 1700326.
- [52] N. Nie, L. Zhang, J. Fu, B. Cheng, J. Yu, Self-assembled hierarchical direct Z-scheme g-C<sub>3</sub>N<sub>4</sub>/ZnO microspheres with enhanced photocatalytic CO<sub>2</sub> reduction

- performance, *Appl. Surf. Sci.* 441 (2018) 12–22.
- [53] Y. Liu, L. Liang, C. Xiao, X. Hua, Z. Li, B. Pan, Y. Xie, Promoting photogenerated holes utilization in pore-rich  $\text{WO}_3$  ultrathin nanosheets for efficient oxygen-evolving photoanode, *Adv. Energy Mater.* 6 (2016) 1600437.
- [54] Q. Liang, Z. Li, Z. Huang, F. Kang, Q. Yang, Holey graphitic carbon nitride nanosheets with carbon vacancies for highly improved photocatalytic hydrogen production, *Adv. Funct. Mater.* 25 (2015) 6885–6892.
- [55] B. Zhu, P. Xia, W. Ho, J. Yu, Isoelectric point and adsorption activity of porous  $\text{g-C}_3\text{N}_4$ , *Appl. Surf. Sci.* 344 (2015) 188–195.
- [56] Y. Kang, Y. Yang, L.C. Yin, X. Kang, G. Liu, H.M. Cheng, An amorphous carbon nitride photocatalyst with greatly extended visible-light-responsive range for photocatalytic hydrogen generation, *Adv. Mater.* 27 (2015) 4572–4577.
- [57] S.I. Boyadjiev, V. Georgieva, N. Stefan, G.E. Stan, N. Mihailescu, A. Visan, I.N. Mihailescu, C. Besleaga, I.M. Szilágyi, Characterization of PLD grown  $\text{WO}_3$  thin films for gas sensing, *Appl. Surf. Sci.* 417 (2017) 218–223.
- [58] P. Xia, B. Zhu, B. Cheng, J. Yu, J. Xu, 2D/2D  $\text{g-C}_3\text{N}_4/\text{MnO}_2$  nanocomposite as a direct Z-scheme photocatalyst for enhanced photocatalytic activity, *ACS Sustain. Chem. Eng.* 6 (2018) 965–973.
- [59] J. Ding, L. Zhang, Q. Liu, W.-L. Dai, G. Guan, Synergistic effects of electronic structure of  $\text{WO}_3$  nanorods with the dominant {001} exposed facets combined with silver size-dependent on the visible-light photocatalytic activity, *Appl. Catal. B* 203 (2017) 335–342.
- [60] J. Fu, C. Bie, B. Cheng, C. Jiang, J. Yu, Hollow  $\text{CoS}_x$  polyhedrons act as high-efficiency cocatalyst for enhancing the photocatalytic hydrogen generation of  $\text{g-C}_3\text{N}_4$ , *ACS Sustain. Chem. Eng.* 6 (2018) 2767–2779.
- [61] J. Liu, B. Cheng, J. Yu, A new understanding of the photocatalytic mechanism of the direct Z-scheme  $\text{g-C}_3\text{N}_4/\text{TiO}_2$  heterostructure, *Phys. Chem. Chem. Phys.* 18 (2016) 31175–31183.